Electrochemical strategy for high-resolution nanostructures in laser-heat-mode resist toward next generation diffractive optical elements

Zhengwei Wang, Guodong Chen, Ming Wen*, Xutao Hu, Xing Liu, Jingsong Wei*, Qingsheng Wu, YongQing Fu

Dr. Z. Wang, G. Chen, X. Liu, Prof. J. Wei
Laboratory of Micro-Nano Optoelectronic Materials and Devices, Shanghai Institute of Optics and Fine Mechanics, Chinese Academy of Sciences, Shanghai 201800, China
Center of Materials Science and Optoelectronics Engineering, University of Chinese Academy of Sciences, Beijing 100049, China
E-mail: weijingsong@siom.ac.cn
Prof. M. Wen, X. Hu, Prof. Q. Wu
School of Chemical Science and Engineering, Shanghai Key Laboratory of Chemical Assessment and Sustainability, State Key Laboratory of Pollution Control and Resource Reuse, Tongji University, Shanghai 200092, China.
E-mail: m_wen@tongji.edu.cn
Prof. Richard Y.Q. Fu
Faculty of Engineering and Environment,
Northumbria University,
Newcastle upon Tyne NE99, UK

Abstract: For achieving high-resolution nanostructures for next generation diffractive optical elements (DOEs) using an environmentally friendly process, we propose and develop an electrochemical development strategy using AgInSbTe based laser heat-mode resist (AIST-LHR). Based on electrical resistivity difference of amorphous and crystalline phases for this resist, an etching selectivity ratio of ~30:1 (i.e., the etch ratio between the amorphous and

crystalline ones) is achieved through the oxidation of Fe^{3+} ions with the assisted pitting activation etching using Cl^- ions in an acid medium. Nanostructures with a minimum feature size down to 41 nm have successfully been generated, including grating patterns, meta-surface optical structures, gears and language characters. Using a post-plasma etching process, the nanostructures are successfully transferred from the AIST-HLR onto silica substrate, and X-ray grating patterns with line space of 80 nm have been created as a demonstration for its potential applications in DOEs.

Keywords: Electrochemical development, high-resolution lithography, AgInSbTe laser heat-mode resist, ~~optical diffraction device~~ diffractive optical elements

1. Introduction

Diffractive optical elements (DOEs) are applied in various fields such as holographic recording media,[1-3] diffractive surface gratings,[4,5] photonic crystal color pixels of sensors,[6,7] spatial light modulators,[8,9] and meta-surfaces.[10-11] For these applications, high-resolution feature sizes and low-cost but highly precision processes are critically demanded. Laser heat-mode lithography, a non-diffraction-limited and maskless direct laser writing (DLW) technique, can be used to fabricate large-area micro/nanostructures.[12-16] Various inorganic laser heat-mode resists (LHRs), such as AgInSbTe (AIST), SbTe, and GeSbTe, are commonly used in the lithography process.[14-19] Among them, AIST is preferred due to its rapid and stable phase transformation.[20-22] In a standard process of laser heat-mode lithography, a laser spot is focused onto the AIST resist. Its phase is changed from an amorphous phase to a crystalline one, which can be used to generate various micro-/nanoscale patterns. The development of the AIST resist is generally carried out in a solution of 17% ammonium sulfide.[23,24] However, hydrolysis of the ammonium sulfide releases toxic and corrosive hydrogen sulfide gas, which causes serious air pollution and potential dangers to operators. Furthermore, this photoresist development process not only has a low etching rate,

but also generates inhomogeneous structures. Therefore, it is critically required to develop a new solution which is not only environment-friendly, but also efficiently develops arbitrary and high-resolution micro/nanostructures.

The AIST contains four metal elements (i.e., Ag, In, Sb, and Te), and thus it is an arduous task to find a desirable developer which can effectively etch all these elements in the AIST. Owing to the high oxidation potentials of Fe^{3+}/Fe^{2+} (ϕ Fe^{3+}/Fe^{2+}, +0.771V), Fe^{3+} ions can oxidize many metals in an acid medium,[25] and thus can be applied to etch the AIST-LHR. In an acid medium with the excessive ions of Cl^-, these Cl^- ions can act as a promotor for pitting activation, thus effectively removing the passivation layers.[26] On another matter, the amorphous AIST has a short-range order and a low electrical resistivity. After its crystallization, the AIST exhibits a long-range order and a significantly increased electrical resistivity.[27] The differences of its electrical resistivities at different phases cause the different etching rates in the solution. Hence, modifying the electrochemical reactions during the development could be applied as a new strategy to achieve high-resolution arbitrary nanostructures using the AIST-LHR in the $FeCl_3$ solution.

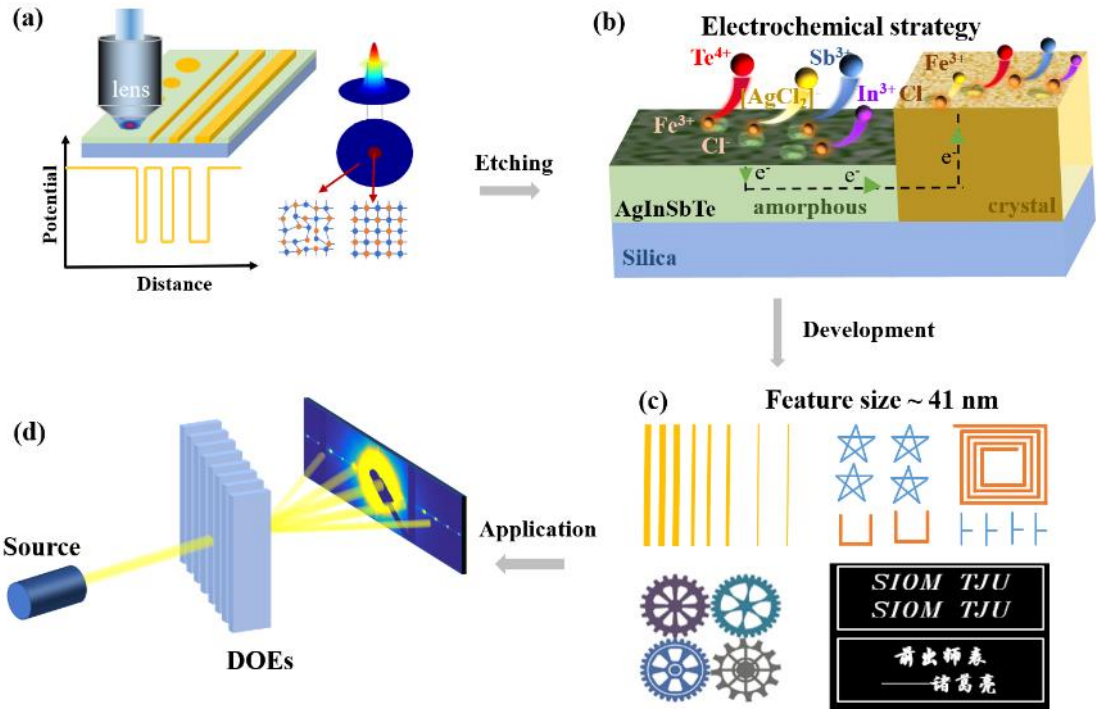

Figure 1. Design and fabrication of high-resolution arbitrary micro/nano-structures: (a) exposure of arbitrary patterns with three-dimensional temperature distribution on the surface of AIST film and corresponding potential distribution; (b) electrochemical development process; (c) various arbitrary structures of AIST-LHR; (d) fabrication of DOEs via plasma etching.

In this paper, we propose an environment-friendly electrochemical development strategy to achieve high-resolution arbitrary patterns using the AIST-LHR. In an acid medium, Fe^{3+} ions are introduced into the developer and Cl^- ions are added into the promotor. They can etch the amorphous phase and crystalline phase of the AIST-LHR with different rates, and a good etching selectivity ratio up to ~30:1 can be achieved between the amorphous and crystalline phases. Using this new strategy, high-resolution and arbitrary structures with a minimum feature size of 41 nm have been successfully obtained, including grating patterns, meta-surface optical structures, various gear, language characters (both English and Chinese). For demonstration of its potential applications in the diffractive optics, a subsequent plasma etching process is applied to create a high-resolution DOE structures.

2. Results and discussion

2.1. Fabrication strategy

In the fabrication process (Figure 1), the DLW system is used to focus the laser beam onto AIST-LHR surface (Figure 1a), which results in the increase of its temperature and crystallization of the laser-irradiated (exposed) region (SI, Figure S1). Because the size of crystallized region is mainly affected by the distribution of laser heat field, it can be much smaller than the size of laser spot by controlling the time and power of laser radiation on the AIST surface. In order to achieve high-resolution arbitrary micro/nano-structures, a new development strategy is performed in the $FeCl_3$ acid solution to selectively etch the amorphous phase and crystalline phases. The mechanism for this process is illustrated in Figure 1b.

Because the electrode potential of $E(Fe^{3+}/Fe^{2+})$ (0.771V) is higher than those of $E(Ag^{+}/Ag)$, $E(In^{3+}/In)$, $E(Sb_2O_3/Sb)$, or $E(TeO_2/Te)$, the four metal elements in the AIST-LHR can be gradually dissolved according to the following reactions.

For Ag: $Ag + Cl^- \rightarrow AgCl \downarrow + e \qquad E = 0.22233\,V$ (1)

$$AgCl + Cl^- \leftrightarrow [AgCl_2]^- \quad (2)$$

AgCl precipitates can be converted into soluble product of $[AgCl_2]^-$ with the excess Cl^- ions.

For In: $In \rightarrow In^{3+} + 3e \qquad E = -0.3382\,V$ (3)

Elements of In can be oxidized into In^{3+} ions which are stable in the In solution.

For Sb: $2Sb + 3H_2O \rightarrow Sb_2O_3 + 6H^+ + 6e \qquad E = 0.152\,V$ (4)

$$Sb_2O_3 + 6H^+ \rightarrow 2Sb^{3+} + 3H_2O \quad (5)$$

Sb can be oxidized into Sb_2O_3, and then dissolved in the acidic condition which is rich in Cl^-.

For Te: $Te + 2H_2O \rightarrow TeO_2 + 4H^+ + 4e \qquad E = 0.593\,V$ (6)

$$TeO_2 + 4H^+ \leftrightarrow Te^{4+} + 2H_2O \quad (7)$$

Te is eventually oxidized and dissolved in the acidic and Cl^- environment.

Additionally, different electrical resistivities between its laser beam-exposed (crystalline) and unexposed (amorphous) regions cause large differences in their electrode potentials. To verify this, a Kelvin probe force microscope (KPFM) was used to characterize the surface potential changes on the AIST-LHR after laser beam exposure (SI, Figure S2). There is a clear difference in the work functions of amorphous and crystalline phases, which are linked to their differences in charge transfer properties. During the development process, the amorphous and crystalline phases can be considered as two metallic electrodes, which are immersed in an electrolyte solution containing the depolarizer (Fe^{2+}/Fe^{3+}) to form a short-circuit primary battery (Figure 1b). When the amorphous and crystalline phases are in contact, current density of anodic dissolution for the amorphous phase of the AIST-LHR is increased significantly. Therefore, electrode potential of the amorphous phase is increased, thus increasing its dissolution rate. In contrast, the electrode potential of crystalline phases is

decreased. Therefore, the overpotential of anodic dissolution reaction of crystalline phases is decreased after contacting with the amorphous phase, thus reducing anodic corrosion rate of the crystalline phases. Clearly using this new electrochemical development strategy; the differences of electrode potentials cause a significantly enhanced etching selectivity between amorphous and crystalline phases of the AIST-HLR, thus achieving high-resolution nanostructures (Figure 1c).

Furthermore, the developed AIST-HLR can be effectively used as a mask for post-dry etch process. Based on the proposed electrochemical development strategy using the AIST-LHR and a standard plasma etching process, a high-resolution silica ~~diffraction grating device~~ DOE (Figure 1d) is fabricated, and its quality is comparable to those made using the focused ions beam lithography.

2.2. Lithographed nanostructures

Using the conventional photolithography with a light wavelength λ of 405 nm and a numerical aperture of NA=0.8, it is difficult to achieve a structure with a feature size D smaller than 618 nm based on the equation of D=(1.22×λ)/NA. Figure 2(a) shows scanning electron microscope (SEM) images of various high-resolution structures, which were obtained using the conventional photolithography method. Using a conventional positive-photoresist such as S1805, widely used in h-line or g-line lithography, can hardly achieve the nanostructures with a minimum feature size about 0.5 μm [28]. Whereas the feature size of AIST-LHR is mainly determined by the distribution of temperature field during the laser beam exposure process, but not by the Abbe diffraction limit for the photolithography[22]. Using the AIST-LHR, we can precisely control the temperature fields using the laser beam, and thus nanoscale crystallized patterns can be easily realized. Using our newly proposed electrochemical development strategy, it is possible to achieve large-scale and high-resolution nanostructures with feature sizes ranging from nanoscale to microscale, e.g., with

periods/linewidths from microscale (2 μm/1 μm), down to nanoscale (400 nm/200 nm and 300 nm/80 nm) as demonstrated in Figures 2b-d. High-resolution meta-surface optical structures have also been successfully fabricated, including helically chiral structure, split-ring structure, hollow star-like structure, and three rotationally symmetrical structure (Figures 2e-h). The minimum line-width we have achieved in this study is ~41 nm. Furthermore, various arbitrary nanostructures, e.g., various gear patterns and different language characters (including English and Chinese) have been successfully created (Figures 2i-k).

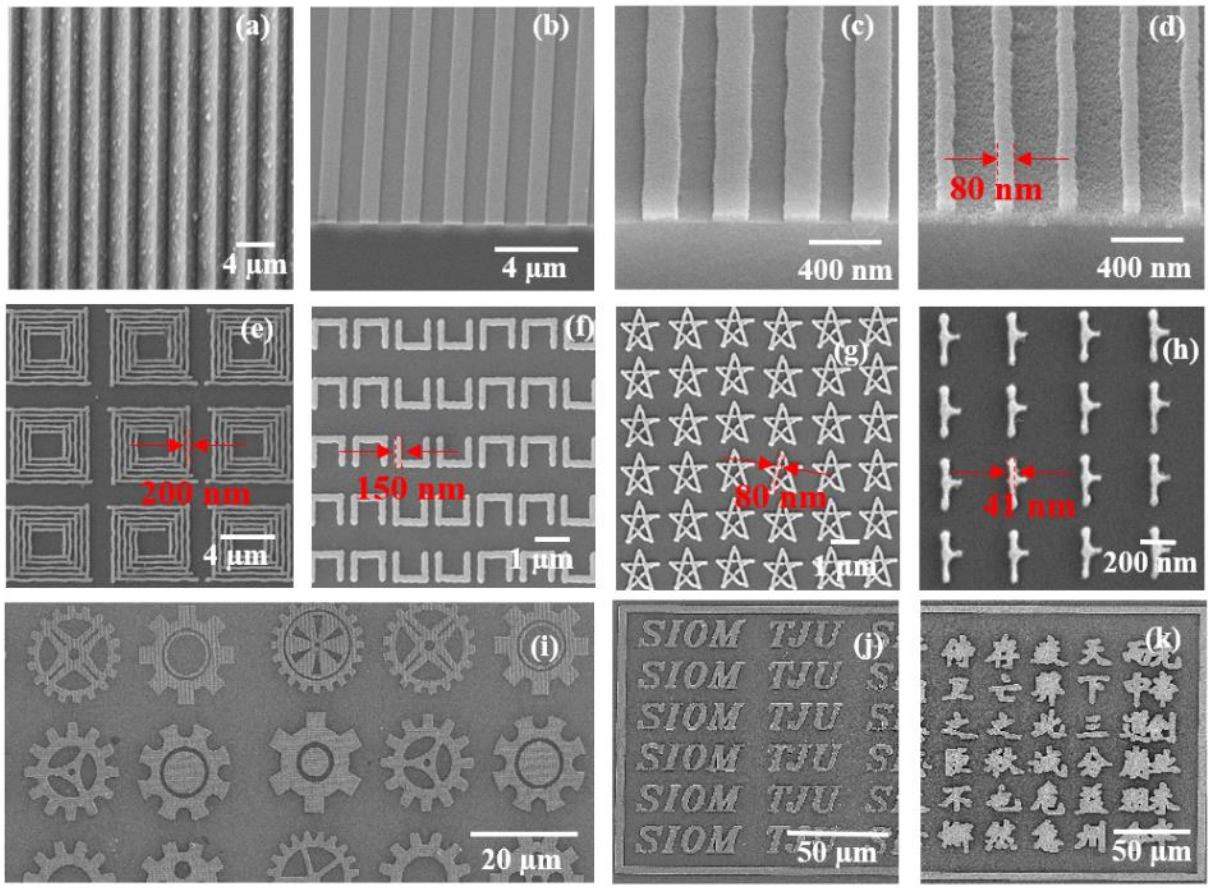

Figure 2. SEM images of various micro/nanostructures (9 mm^2 on the silica substrates). (a) produced from a conventional photoresist (S1805) with the developed gratings period/linewidth of 3 μm/1 μm; (b) AIST-LHR patterns after electrochemical developing with gratings having period/linewidth of 2 μm/1 μm; (c) 400 nm/200 nm features; and (d) 300 nm/80 nm features; multi-functional meta-surfaces for optical structures including helical chiral (e), split-ring(f), hollow star-like(g), and three rotational symmetry(h) structures with the feature size of 41 nm ; arbitrary cross micro-/nanoscale various gear patterns (i), English (j) and Chinese characters (k).

2.3. Mechanism of electrochemical development

To understand the wet-etching (or developing) mechanisms for using $FeCl_3$ to etch the AIST-LHR, we investigate the characteristics of the electrochemical development. Electrode potential, etching current and impedance of the AIST-HLR during its development process have been studied in detail. Figures 3a-b show the obtained electro-potential polarization curves of the amorphous and crystalline AIST-LHR in different concentrations of $FeCl_3$ solutions. Their corresponding fitting parameters are listed in Table S1. As shown in Figure 3c, when the concentration of $FeCl_3$ solution is lower than 0.5 and 1.2 $mol \cdot L^{-1}$, their etching potentials are increased with the increase of $FeCl_3$ concentration, whereas their etching current densities are decreased due to the formation of a surface passivation layer. Further increase of the $FeCl_3$ concentration leads to a downward trend of etching potentials, whereas the etching current density is increased sharply. This is mainly because the increase of Cl^- concentration enhances the pitting reactions, thus removing the passivated layer.[29]

Spectra of electrochemical impedance spectroscope (EIS) show two capacitive arcs in different solution concentrations for the amorphous and crystalline phases, respectively (Figures 3d-e). The high-frequency band of capacitive arcs is related to the double-layer capacitance (C_{dl}) and charge-transfer resistance (R_{ct}), and the low-frequency band one is related to resistance (R_p) of the corrosion product layer formed on the surface of AIST-LHR. The capacitance resistance increases with an increase in the $FeCl_3$ concentration because of the formation of a passivation layer on the surface. As the concentration of $FeCl_3$ is continually increased to 0.5 or 1.2 $mol \cdot L^{-1}$ for the amorphous or crystalline phases, respectively, the passivation layer disappears. The reaction is changed from a dynamic control mode to a substance diffusion control mode, which causes the increased diffusion resistance (W).[30]

The equivalent circuit diagrams (Figure 3f) are proposed and used to fit the electrochemical impedance data, where R_s is the solution resistance and C_p is the corrosion product layer capacitance. The corresponding impedance-fitting parameters are listed in Table S2. Results

confirm that the impedance values of the crystalized phase are larger than those of the amorphous phase, thus more etching products are adhered to surface of amorphous phase. Using a $FeCl_3$ solution of 0.5 mol·L^{-1} for about 60 s, the increase of etching current density results in the increase of the height of amorphous area compared with the crystalline area (Figure 3g), and the etching products are adhered to surface to form a passivation layer. Whereas using a higher $FeCl_3$ concentration, this passivation layer is dissolved. The development morphologies obtained at durations of 10 and 30 s (Figure 3h-i) with a solution concentration of 1.2 mol·L^{-1} show that the height of crystalline region is larger than that of the amorphous region. A pitting morphology caused by Cl^- ions can be clearly seen in Figure 3i.

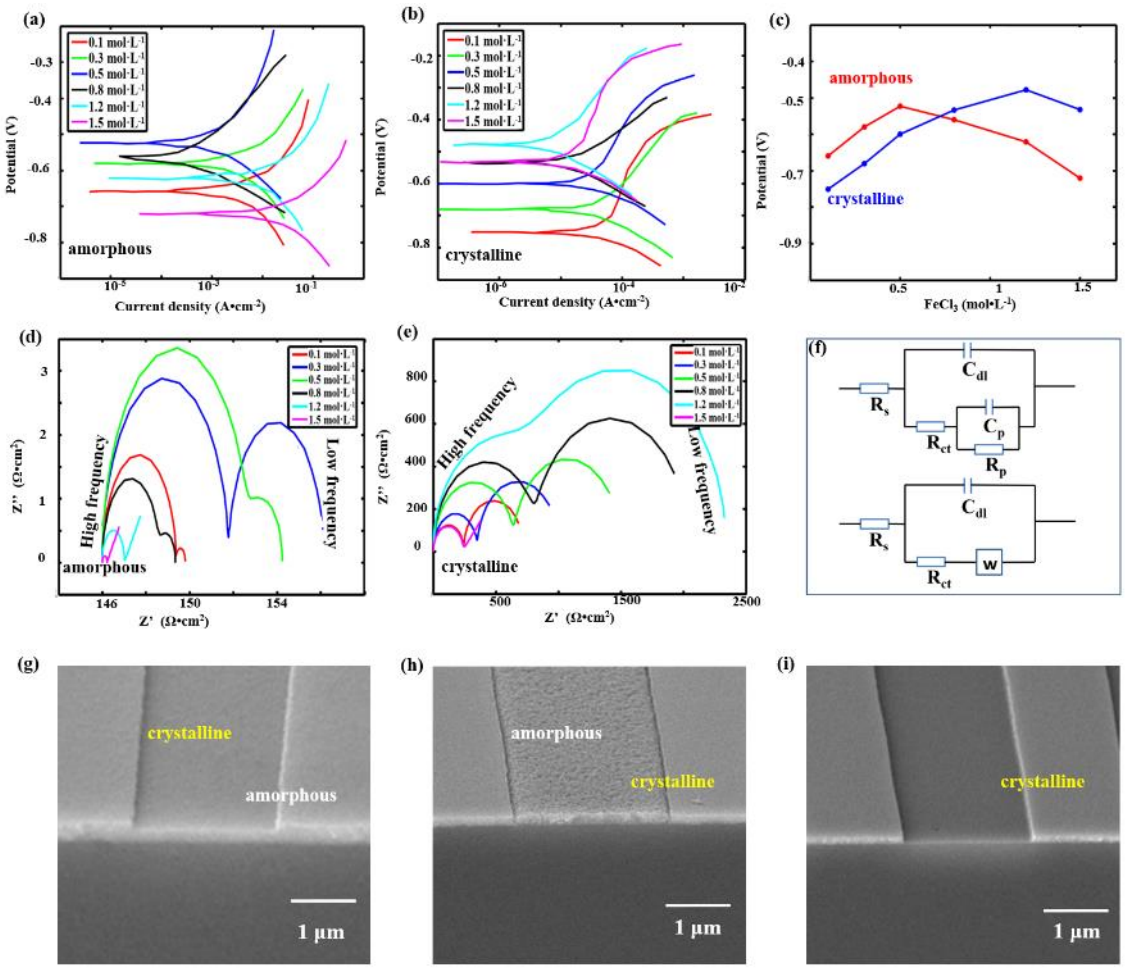

Figure 3. (a, b) Polarization curves of amorphous and crystalline AIST-LHR with the size of 9 mm^2; (c) Etching potential trends of amorphous and crystalline AIST-LHR with the sample size of 9 mm^2; (d, e) Impedance spectrum curves of amorphous and crystalline AIST-LHR with the sample size of 9 mm^2; (f) Fitted circuit diagram; SEM images with the sample size of 9 mm^2 obtained at 0.5 mol·L^{-1} $FeCl_3$ for 60 s (g), of 1.2 mol·L^{-1} $FeCl_3$ for 10 s (h) and 30 s (i), respectively.

In summary, due to the difference of potentials between the crystalline and amorphous electrodes, they exhibit different etching rates in the development prcoess. At a lower concentration of $FeCl_3$, the etching current density of the amorphous region is greater than that of the crystalline region, and the etching products are adhered to the film surface to form a passive layer. At this moment, the height of amorphous region is higher than that of crystalline region, but it cannot be used as a good photoresist (or it can not form a good window-like structure). As the concentration of $FeCl_3$ is increased, the passive film layer disappears, and the corrosion rate of the amorphous region is higher than that of the crystalline region, which makes the height of crystalline region much higher than that of amorphous region, thus completing the electrochemical development.

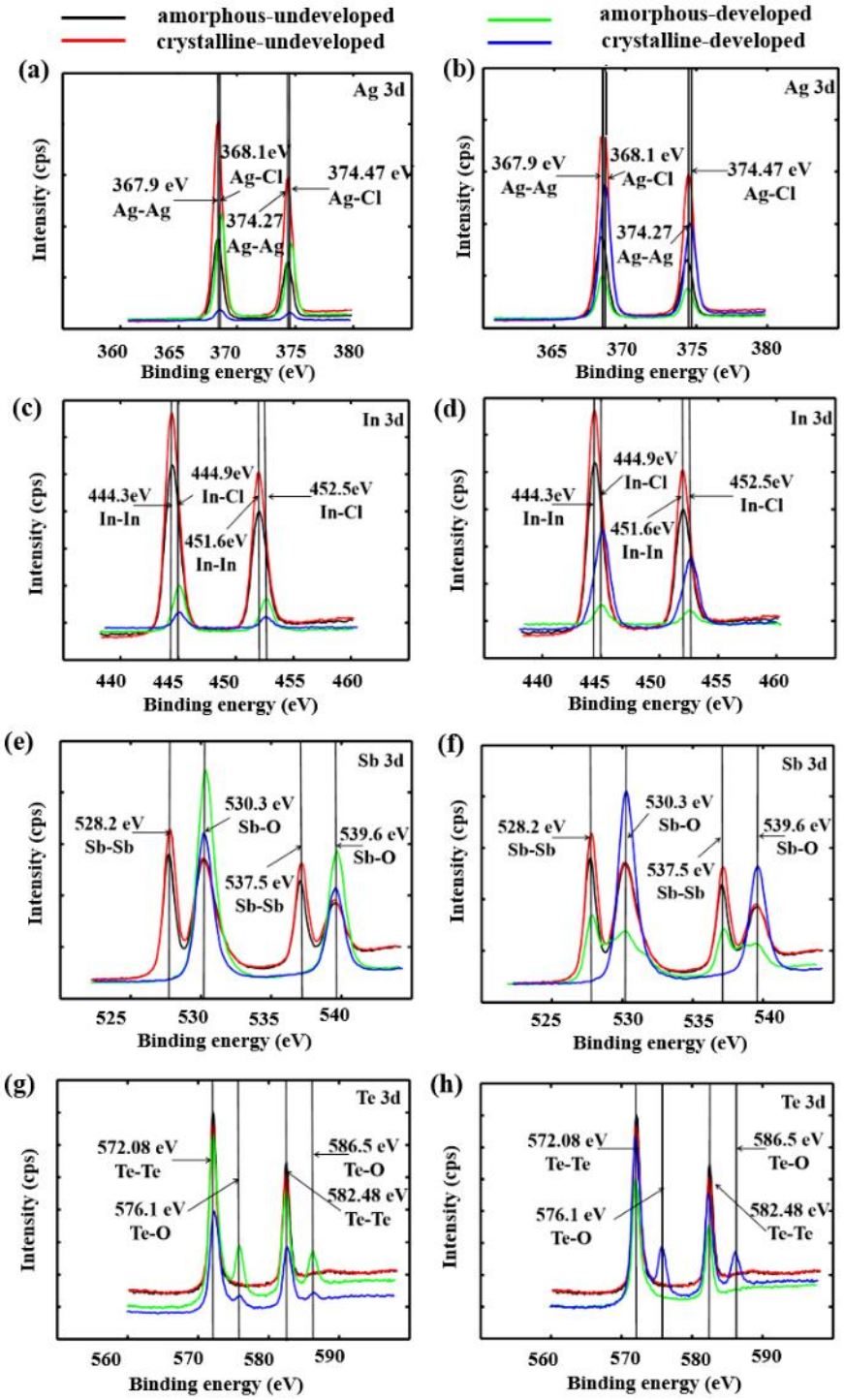

Figure 4. XPS analysis of amorphous developed, amorphous undeveloped, crystalline developed and crystalline undeveloped samples with the size of 9 mm^2. The results of Ag 3d (a, b), In 3d (c, d), Sb 3d (e, f), and Te 3d (g, h) are obtained at 0.5(left) and 1.2 $mol \cdot L^{-1}$(right), respectively.

To verify the changes of surface etching chemistry, analysis using an X-ray photoelectron spectroscope (XPS) was performed, and the obtained results are shown in Figure 4. In Figure 4a, Ag 3d peaks of AIST-LHR are identified at 367.9 and 374.27 eV, respectively,

corresponding to $3d^{5/2}$ and $3d^{3/2}$ Ag-Ag bonds.[31] However, these peaks are disappeared after the resist is etched in 0.5 mol·L^{-1} $FeCl_3$ solution, whereas new peaks are identified at 368.1 and 374.47 eV, which are corresponding to those of Ag-Cl bonds. These peaks are significantly higher for the amorphous phase than that for the crystalline phase.[32] The Ag-Cl bonds are identified in the crystalline phase even at a high concentration (1.2 mol·L^{-1}) of the $FeCl_3$ solution. The AgCl was further converted into soluble product of $[AgCl_2]^-$ when the Cl^- ions are excessive in the solution (Figure 4b). Meanwhile, the Ag-Ag bonds are detected in the amorphous phase due to the disappearance of passivation layer. For the In 3d, the peaks at 444.3 and 451.6 eV are corresponding to the $3d^{5/2}$ and $3d^{3/2}$ peaks of In-In bonds (Figures 4c-d) for both the crystalline and amorphous ones, respectively,[33] indicating that they are mainly existed as In-In bonds before etching.[34] Whereas after etching, a weak In-Cl bond appears. In Figures 4e-f, the Sb $3d^{5/2}$ and Sb $3d^{3/2}$ peaks of the Sb-Sb bonds are at 528.2 and 537.5 eV, respectively.[35] Their oxidation bond energies are 530.3 and 539.6 eV,[36] both of which are corresponding to those of Sb-O bonds. The Sb-Sb bonds disappear when the etching occurs at 0.5 mol·L^{-1} $FeCl_3$ solution, because Sb is oxidized into Sb_2O_3. While at 1.2 mol·L^{-1} solution, the Sb-Sb bonds can still be detected in the amorphous phase, owing to the disappearance of the passivation layer. Figures 4g-h show the peaks of Te 3d at 572.08 and 582.48 eV, corresponding to the homopolar bonds of Te-Te.[37] The Te-O bond appears after wet etching in a 0.5 mol·L^{-1} $FeCl_3$ solution due to the oxidation of Fe^{3+}.[38] However, this bond disappears in a 1.2 mol·L^{-1} $FeCl_3$ solution, which indicates the disappearance of the passivation layer.

Comparatively, etching in the 0.5 mol·L^{-1} $FeCl_3$ solution results in the larger height of amorphous area than that of crystalline area, which shows the characteristics of a positive resist. Whereas etching in the 1.2 mol·L^{-1} $FeCl_3$ solution shows the characteristics of a negative resist, i.e., obtaining a lower height of amorphous area than that of crystalline area (SI, Figure S4-S5).

In brief, the etching rate of the amorphous phase is much higher than that of the crystalline phase, which can be explained by the reaction kinetics. The rate constant k_c of a chemical reaction can be expressed as:

$$k_c = \frac{kT}{\hbar} \exp\left(-\frac{-\Delta G^*_{A\to C}}{RT}\right) \quad (8)$$

where *k* is the Boltzmann constant, *h* is the Planck constant, *R* is the Avogadro constant, *T* is the temperature, and $\Delta G^*_{A\to C}$ is the activation energy of amorphous to crystalline phases. The amorphous phase has a short-range ordered lattice structure.[39] There are more unbounded electrons in the amorphous phase, which makes it easier to lose electrons during the electrochemical reactions. Therefore, the amorphous phase only needs a lower activation energy to generate active particles and trigger the electrochemical reactions. When the film is crystallized, the system is in a much more stable stage, without many unpaired electrons. Therefore, a much higher activation energy is required to initiate the reaction, thus the etching rate of the crystalline phase is much lower than that of the amorphous phase.

2.4. Key influencing factors for development

We have further studied the variations in reaction speeds and selective etching ratios with the concentration of $FeCl_3$ solution, based on the measured structure's heights after development. The obtained results are shown in Figure 4a. In these cases, an etching ratio less than 1 indicates that the height of amorphous region is larger than that of crystalline region, which links to the characteristics of a positive resist. Whereas if the etching ratio is larger than 1, it indicates that the height of crystalline region is larger than that of the amorphous region, showing the characteristics of a negative resist. In this study, when the concentration of $FeCl_3$ solution is lower than 1.2 mol·L^{-1}, the etching selectivity ratio is increased from ~1 to ~30 with an increase of $FeCl_3$ concentration from 0.1 mol·L^{-1} to 1.2 mol·L^{-1}. With a concentration of 1.2 mol·L^{-1}, the etching rates of the amorphous and crystallization phases are 3.0 and 0.1

nm/s, respectively, which is corresponding to an etching selection ratio of ~30:1. This shows that the AIST-LHR has an excellent etching selectivity.

During the developing process, it is critical to understand the effect of Cl^- ions on the etching selectivity at different Fe^{3+} concentrations. The NaCl was selected to add into the solution in order to adjust the concentration of Cl^- in the developer. Figure 4b shows the obtained relationships among Cl^- concentration, etching selectivity ratio, and reaction rate at a Fe^{3+}concentration of 1.2 mol·L^{-1}. Results show that with the increase of Cl^- concentration, the etching selectivity ratio is gradually decreased, and the reaction rate is increased accordingly. Whereas when the Cl^- concentration is further increased to 4.6 mol·L^{-1}, the selective corrosion ratio is decreased to ~3:1. This is mainly because the further increase of Cl^- concentration accelerates the pitting activation etching and depassivation of the crystalline region, along with the increase of surface roughness (Figure 4c). Owing to the enhanced pitting effect of Cl^- ions on the film, excessive edge roughness of the obtained patterns can be observed. Therefore, the concentration of Cl^- ions should be controlled as low as possible, in order to minimize the edge roughness during the developing process.

Additionally, because of the existence of hydrolysis reactions of Fe^{3+}, with the increase of etching time, a large amount of $Fe(OH)_3$ precipitates are produced in the developing solution, which affects the diffusion of Fe^{3+}, thus causing a large amount of development defects (Figure 5d). The color change (inset of Figure 5d) of $FeCl_3$ solutions (1.2 mol·L^{-1}) before and after adding 0.1 mol·L^{-1} HCl reveals that the solution is transformed from a turbid phase into a clear one, which can effectively reduce the hydrolysis of Fe^{3+}. Therefore, to improve the stability of the development process, a mixed solution of 1.2 mol·L^{-1} $FeCl_3$ and 0.1 mol·L^{-1} HCl should be used to prevent the formation of impurity ions in this study. Besides the above two key influencing factors (i.e., the concentration of $FeCl_3$ solution and the concentration of Cl^-), uniformity of development structure obtained at different duty cycles was also investigated. The detailed results are shown in the SI (Figure S6-S9). The uniformity of

linewidth and depth can be well controlled by adding appropriate etching additives (e.g., di-hydroxyethyl water-solubility imidazoline) and surfactants (e.g., sodium dodecyl sulfate) during the electrochemical development.

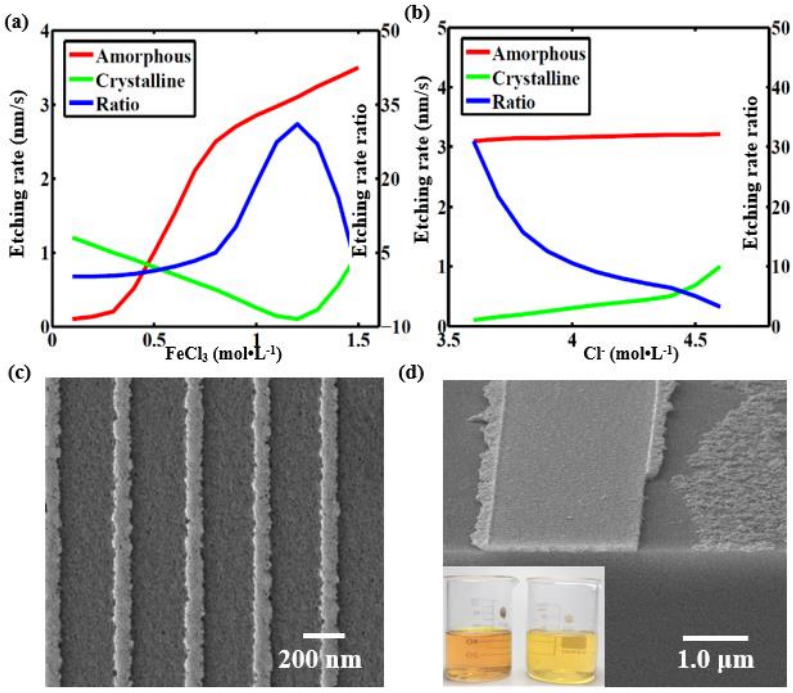

Figure 5. (a, b) The variation trend of etching rate amorphous and crystalline phases and selection ratio of with the concentration of $Fe^{3+}$and Cl^-, respectively; (c) SEM image with a sample size of 9 mm^2 of one obtained at Cl^{-1} concentration of 4 $mol \cdot L^{-1}$ for understanding the effect of Cl^- on the roughness of line edges; (d) Effect of pH on surface morphology.

2.5. Demonstration for fabrication of a~~n optical diffraction grating~~a DOE

In this section, we will apply the electrochemical development strategy to demonstrate the fabrication of a a~~n X-ray grating~~DOE on the silica substrate, for diffractive optics applications. As shown in Figure 2d, the obtained feature size of the fabricated AIST-LHR on the silica is 80 nm and the pitch is 300 nm. Through the following etching process with SF_6 and O_2 plasma, the structures are successfully transferred onto the silica. Figure 6a shows an image of the fabricated grating with a functional area of ~120 mm × 100 mm. As demonstrated in Figure 6b, the grating lines have been etched with a depth of ~500 nm.

The fabricated grating using the newly proposed electrochemical development strategy is characterized using X-rays. When the X-ray beam passes through this diffraction grating, it is

split up into a central bright beam plus a number of side beams. A detector was employed to measure the beams intensity. With a beam energy of 10 keV and a record time of 0.1 s, we randomly measured the intensity of the $+1_{st}$ order beam and selected 6×6 points in the whole device, in order to check the uniformity of the whole grating pattern. The obtained results are shown in Figure 6c. The average $+1_{st}$ order beam intensity distribution in each region is ~4500, and the intensity of each region is quite consistent, revealing that the grating has a good uniformity. Figures 6d-e show the diffraction results of one of the points and the corresponding intensity distributions of -6_{th} to $+6_{th}$ order beams (with a recording time of 1s and sheltered 0th-order and part of 1st-order beams). The appearance of split beams with different diffraction orders clearly demonstrates that the fabricated grating is effective in light splitting.

Furthermore, the diffraction efficiencies of the fabricated grating were tested and the obtained results are shown in Figure 6f. We calculated the theoretical diffraction efficiency using the publicly available data from the Berkeley Laboratory Centre for X-ray optics (http://henke.lbl.gov/). The calculated and measured results match well. All these results clearly prove that the electrochemical development strategy is effective for preparation of high-resolution optical device. However, we should address that the efficiency is still relatively low, mainly due to the high absorption of X-rays by silica.

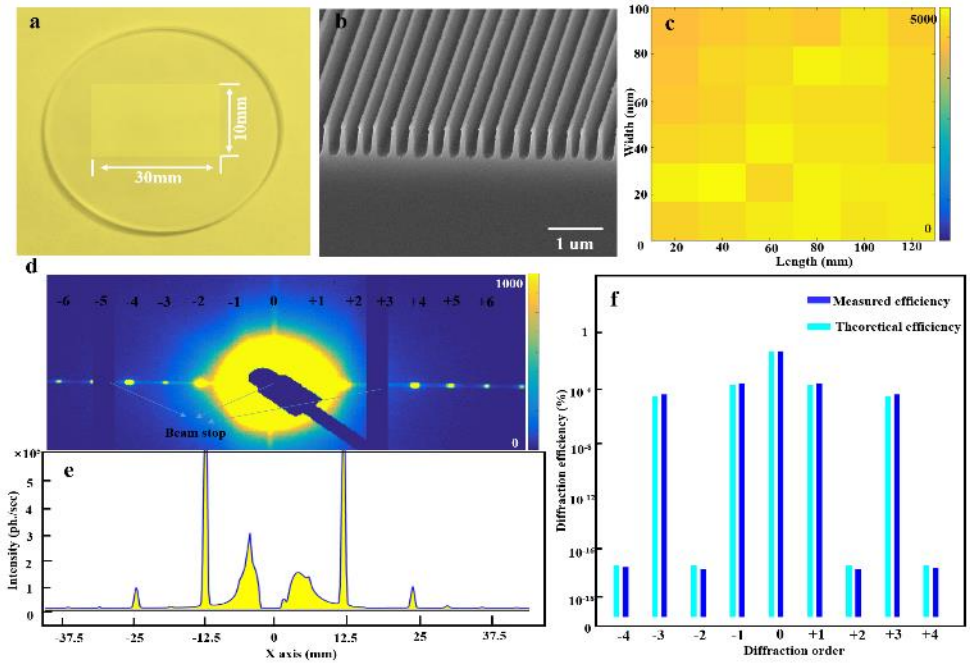

Figure 6. Results of fabricated ~~grating~~ DOE through electrochemical developed AIST-LHR. (a) Photograph of the fabricated grating on the silica substrate, (b) cross sectional SEM image of fabricated grating with the sample size of 30 mm×10mm, (c) 1_{st} order beam intensity map of the grating measured with 10 keV X-rays, (d) detector spatial data showing the grating diffraction at a distance of 21 m downstream of the grating, (e) intensity line profile from the detector image across the grating diffraction orders up to the 6_{th}, (f) Measured and theoretical diffraction efficiency of different diffraction order (-4^{th} to $+4^{th}$).

3. Conclusions

In summary, this work research a new electrochemical methodology to realize high-resolution and arbitrary patterns of AIST-LHR through the oxidation of Fe^{3+} ions with the assisted pitting activation etching using Cl^- ions in an acid medium. Using the optimized concentration of Fe^{3+} and Cl^- ions, an etching ratio of amorphous vs. crystalline regions up to ~30:1 can be achieved with a minimized feature size of ~41 nm. The inhomogeneity of development process, which is mainly caused by galvanic etching and surface hydrophilicity, can be effectively minimized by applying the additives and surfactants. A~~n optical diffraction device~~ A DOE of an X-ray grating is fabricated using the AIST-LHR, and show good uniformity and diffraction properties. Electrochemical development based on laser heat-mode lithography is an environment friendly method which produces large scale, uniform, high-resolution and arbitrary micro and nanostructures.

4. Experimental procedures

Preparation of amorphous AIST-LHR: An 80 nm thick AIST was deposited using a magnetron sputtering system (JPG 560) on quartz glass (SiO_2, 99.0%, Φ30 mm, thickness: 1 mm) with an area of 9 cm^2 and a thickness of 1.3 mm. The obtained film was amorphous. The background pressure of the deposition chamber was less than 6.0×10^4 Pa, the sputtering power was 40 W, and the working pressure was 0.8 Pa under an Ar atmosphere.

Exposure and development: A lithography system, using a laser beam to induce thermal exposure in both vector and scalar modes, was used for patterning AIST-LHR. The wavelength was 405 nm and the numerical aperture of the objective lens was 0.8. The corresponding theoretical spot size was 0.62 μm. At room temperature and under the atmospheric environment, the patterned sample was immersed in the developer solution for development, after which the samples were washed with deionized water and dried with N_2.

Characterization: Surface morphology of the structures was characterized using an atomic force microscope (AFM, Veeco, Multi-mode V, America), SEM (Carl Zeiss, Zeiss Auriga, Germany), TEM and high-resolution TEM (HRTEM, JEM-2100EX microscopy, Japan), and an optical microscope (OM, Olympus, BX51, Japan). Crystalline structures of the materials were evaluated using an XRD (PANalytical, Empyrean, Netherlands) with a Cu Kα radiation source (γ=0.154056 nm). Element analysis was carried out using an energy disperse X-ray spectroscopy (EDS, Oxford, TN5400, Britain) conducted at 15 keV. Elemental and chemical binding structures were obtained using an XPS (Thermo Fisher Scientific, K-ALPHA, America) with Al Kα radiation with an energy of 1486.6 eV. Binding energies were calibrated using the peak of the contaminate carbon (C 1s=284.6 eV).

Electrochemical experiment: Electrochemical behavior of the AIST in the $FeCl_3$ solution was studied using an electrical potentiometric polarization method with a CH1760E electrochemical workstation. The reference electrode was a saturated calomel. The auxiliary electrode was a platinum electrode. The experimental temperature was maintained at 25℃.

The sample was immersed in the $FeCl_3$ solution until the potential was stabilized. The potential was scanned from the cathodic to the anodic with a scanning range of -0.2 to 0.2 V and a scanning speed of 0.5 mV/s. The corrosion potential, E_{corr}, and the corrosion current density, I_{corr}, were obtained by fitting the measured polarization curves using the Cview software package. Under the applied potential of the electrode, the EIS data were obtained by scanning from a high frequency of 10000 Hz to a low frequency (0.1 Hz) with a sinusoidal voltage amplitude of 5 mV. The impedance spectrum data were fitted using the ZSimpWin software package, and the electrode property was analyzed according to the equivalent circuit.

Plasma Etching: The pattern transfer from the AIST-HLR to the silica substrate was performed using an RIE equipment (Plasma-Therm, Vision 322, America). The etching parameters were 70 sccm SF_6 flow, 6 sccm O_2 flow, 250 W source power, 20 mTorr chamber pressure, and 20 °C cooling temperature. It was etched for 10 min. After etching, the proposed $FeCl_3$ developer was used to remove the residual AIST-HLR.

Statistical Analysis: An 80 nm thick AIST was deposited using a magnetron sputtering system and the step profile was used to measure the thickness. The substrate was a quartz glass (SiO_2, 99.0%, Φ30±1 mm, thickness: 1±0.1 mm) with a writing area of 9 cm^2 for all of samples. Exposed AIST-LHRs was developed in the $FeCl_3$ solutions of 0.1, 0.3, 0.5, 0.8, 1.2 and 1.5 $mol \cdot L^{-1}$ for 30 seconds for electrical potentiometric polarization examinations. The XPS tests were employed on the AIST-LHR's surfaces which were developed in the 0.5 and 1.2 $mol \cdot L^{-1}$ $FeCl_3$ solution for 30 seconds. The data of impedance spectra were fitted using the ZSimpWin software package, and the electrode property was analyzed according to the equivalent circuit.

Supporting Information

Supporting information is available from the Wiley Online Library or from the author.

Acknowledgements

This work was partially supported by the National Natural Science Foundation of China (Nos. 61627826 and 22171212), Strategic High-Tech Innovation Fund of the Chinese Academy of Sciences (GQRC-19-08), International Corporation Project of Shanghai Committee of Science and Technology by China (21160710300), International Exchange Grant (IEC/NSFC/201078) of Royal Society UK and NSFC. Author 1 (Zhengwei Wang) and Author 2 (Guodong Chen) contributed equally to this work.

Conflicts of interest

The authors declare no conflict of interest.

Received: ((will be filled in by the editorial staff))
Revised: ((will be filled in by the editorial staff))
Published online: ((will be filled in by the editorial staff))

References

[1] Y. Lim, B. Kang, S. J. Hong, H. Son, E. Im, J. Bang, S. Lee, *Adv. Funct. Mater.* **2021**, *31*, 2104105.

[2] Kwangjin Kim, Haedong Park, Kyung Jin Park, Sung Hun Park, Hyeon Ho Kim, Seungwoo Lee, *Adv. Opt. Mater*. **2019**, 1900074.

[3] H. Rekola, A. Berdin, C. Fedele, *Sci. Rep.* **2020**, *10*, 19642.

[4] Y. Lim, H. Park, B. Kang, K. Kim, D. Yang, S. Lee, Holography, *Advanced Photonics Research* **2021**, *2*, 2100061.

[5] N. Lassaline, R. Brechbühler, S.J.W. Vonk, *Nature* **2020**, 582, 506–510.

[6] K. J. Park, J. H. Park, J. H. Huh, C. H. Kim, D. H. Ho, G. H. Choi, *ACS Appl. Mate. & Inter.* **2017**, *9*, 9935-9944.

[7] S. J. Yeo, K. J. Park, K. Guo, P. J. Yoo, S Lee, *Adv. Mater.* **2016**, *28*, 5268-5275.

[8] Y. Lim, B. Kang, S. J. Hong, H. Son, E. Im, J. Bang, S. Lee, *Adv. Funct. Mater.* **2021**, *31*, 2104105.

[9] S. L. Oscurato, F. Reda, M. Salvatore, F Borbone, P. Maddalena, A. Ambrosio, *Laser & Photonics Rev.* **2022**, 2100514

[10] K. Hong, J. Yeom, C. Jang, G. Li, J. Hong, B. Lee, *Opt. Express* **2014**, *22*, 14363.

[11] Y. Li, T. Zhan, S.-T. Wu, *Opt. Express* **2020**, *28*, 5875.

[12] C. F. Guo, V. Nayyar, Z. Zhang, Y. Chen, J. Miao, R. Huang, Q. Liu, *Adv. Mater.* **2012**, *24*, 3010.

[13] B. Oktem, I. Pavlov, S. Ilday, H. Kalaycıoğlu, A. Rybak, S. Yavaş, M. Erdoğan, F. O. Ilday, *Nat. Photonics* **2013**, *7*, 897.

[14] H. Xi, Q. Liu, Y. Tian, S. Guo, M. Cu, G. Zhang, *J. Nanosci. Nanotechno.* **2013**, *13*, 829.

[15] Y. Q. Huang, R. Huang, Q. L. Liu, C. C. Zheng, J. Q. Ning, Y. Peng, Z. Y. Zhang, *Nanoscale Res. Lett.* **2017**, *12*, 12.

[16] Z. Gan, Y. Cao, R. A. Evans, M. Gu, *Nat. Commun.* **2013**, *4*, 2061.

[17] K. Zhang, Z. Wang, G. Chen, Y. Wang, A. Zeng, J. Zhu, S. Avakaw, H. Tsikhanchuk, *Opt. Lett.* **2019**, *17*, 093102.

[18] Y. Meng, J. K. Beherac, Z. Wang, J. Zheng, J. Wei, L. Wu, Y. Wang, *Appl. Surf. Sci.* **2020**, *508*, 145228.

[19] M. Salinga, E. Carria, A. Kaldenbach, M. Bornhofft, J. Benke, J. Mayer, M. Wuttig, *Nat. Commun.* **2013**, *4*, 2371.

[20] J. Wei, R. Wang, *J. Appl Phys.* **2014**, *115*, 123102.

[21] Z. Wang, J. Zheng, G. Chen, K. Zhang, T. Wei, Y. Wang, *Adv. Eng. Mater.* **2021**, 2001468.

[22] J. Wei, K. Zhang, T. Wei, Y. Wang, Y. Wu, M. Xiao, *Sci. Rep.* **2017**, *7*, 43892.

[23] Z. Wang, K. Zhang, G. Chen, Z. Zhu, Y. Wang, J. Wei, *Mater. Let.* **2020**, *264*, 127344.

[24] G. Chen, J. Zheng, Z. Wang, *Journal of Alloys and Compounds* **2021**, 158988.

[25] D Fullenkamp, D Barrett, D Miller, Kurutz, J., Messersmith, P., *Rsc Advances*, **2014**, *4*, 25127.

[26] O. Dinard. *Hydrometallurgy*, **1985**, *13*, 345.

[27] T. Matsunaga, J. Akola, S. Kohara, T. Honma, K. Kobayashi, E. Ikenaga, *Nature Materials*, **2011**, *10(2)*, 129-34.

[28] Giorgio A. L. M. Degiorgis, Patrizia Pateri, Alberto Pilenga, Rodney J. Hurditch, Bernard T. Beauchemin Jr., Edward A. Fitzgerald, *Proc. SPIE Advances in Resist Technology and Processing VII*, **1990**, *1262*, 368-377.

[29] A. Malik, P. Kutty, N. Siddiqi, I. Andijani, S. Ahmed, *Corros. Sci.* **1992**, *33*, 1809.

[30] LZ Wang, Y Li, G Zhang, *Corrosion Science* **2019**,*146*, 121-133.

[31] J. C. Fuggle, E. Kallne, L. M. Watson, D. J. Fabian, *Phys Rev B* **1977**, *16*, 750.

[32] V. K. Kaushik, *J. Electron Spectrosc.* **1991**, *56*, 273.

[33] M. Ouchene, C. Senenaud, E. Belin, *Journal of Non-Cryst. Solids* **1983**, *59 & 60*, 625.

[34] G. E. Mcguire, G. K. Schweitzer, Thomas A. Carlson, *Inorg. Chem.* **1973**, *12*, 2450.

[35] R. B. Shalvoy, G. B. Fisher, P. J. Stiles, *Phys. Rev. B* **1977**, *15*, 1680.

[36] R. Delobel, J. Chem. SOC., *Furuday Trans. I* **1983**, *79*, 879.

[37] J. M. Thomas, I. Adams, R. H. Williams, M. Barber, *J. Chem. Soc. Faraday T.* **1972**, *68*, 755.

[38] M. K. Bahl, R. L. Watson, and K. J. Irgolic, *J. Chem. Phys.* **1977**, *66*, 5526.

[39] D. Kim, T. S. Jung, H. Park, W. Yang, J. Han, S. Hwang, K. I. Sim, Y. Kwon, J. H. Kim, M. Cho, *Appl. Surf. Sci.* **2021**, *544*, 148838.

Caption

Figure 1. Design and fabrication of high-resolution arbitrary micro/nano-structures: (a) exposure of arbitrary patterns with three-dimensional temperature distribution on the surface of AIST film and corresponding potential distribution; (b) electrochemical development process; (c) various arbitrary structures of AIST-LHR; (d) ~~optical diffraction grating~~ DOEs fabrication via plasma etching.

Figure 2. SEM images of various micro/nanostructures (9 mm^2 on the silica substrates). (a) produced from a conventional photoresist (S1805) with the developed gratings period/linewidth of 3 μm/1 μm; (b) AIST-LHR patterns after electrochemical developing with gratings having period/linewidth of 2 μm/1 μm; (c) 400 nm/200 nm features; and (d) 300 nm/80 nm features; multi-functional meta-surfaces for optical structures including helical chiral (e), split-ring(f), hollow star-like(g), and three rotational symmetry(h) structures with the feature size of 41 nm ; arbitrary cross micro-/nanoscale various gear patterns (i), English (j) and Chinese characters (k).

Figure 3. (a, b) Polarization curves of amorphous and crystalline AIST-LHR with the size of 9 mm^2; (c) Etching potential trends of amorphous and crystalline AIST-LHR with the sample size of 9 mm^2; (d, e) Impedance spectrum curves of amorphous and crystalline AIST-LHR with the sample size of 9 mm^2; (f)Fitted circuit diagram; SEM images with the sample size of 9 mm^2 obtained at 0.5 $mol \cdot L^{-1}$ $FeCl_3$ for 60 s (g), of 1.2 $mol \cdot L^{-1}$ $FeCl_3$ for 10 s (h) and 30 s (i), respectively.

Figure 4. XPS analysis of amorphous developed, amorphous undeveloped, crystalline developed and crystalline undeveloped samples with the size of 9 mm^2. The results of Ag 3d (a, b), In 3d (c, d), Sb 3d (e, f), and Te 3d (g, h) are obtained at 0.5(left) and 1.2 $mol \cdot L^{-1}$(right), respectively.

Figure 5. (a, b) The variation trend of etching rate amorphous and crystalline phases and selection ratio of with the concentration of $Fe^{3+}$and Cl^-, respectively; (c) SEM image with a sample size of 9 mm^2 of one obtained at Cl^{-1} concentration of 4 $mol \cdot L^{-1}$ for understanding the effect of Cl^- on the roughness of line edges; (d) Effect of pH on surface morphology.

Figure 6. Results of fabricated ~~grating~~ DOE through electrochemical developed AIST-LHR. (a) Photograph of the fabricated grating on the silica substrate, (b) cross sectional SEM image of fabricated grating with the sample size of 30 mm×10mm, (c) 1_{st} order beam intensity map of the grating measured with 10 keV X-rays, (d) detector spatial data showing the grating diffraction at a distance of 21 m downstream of the grating, (e) intensity line profile from the

detector image across the grating diffraction orders up to the 6_{th}, (f) Measured and theoretical diffraction efficiency of different diffraction order (-4^{th} to $+4^{th}$).

The tables of contents entry

Electrochemical strategy for high-resolution nanostructures in laser-heat-mode resist toward next generation ~~diffractive optics~~ diffractive optical elements

Zhengwei Wang, Guodong Chen, Ming Wen, Xutao Hu, Xing Liu, Jingsong Wei*, Qingsheng Wu, YongQing Fu*

Based on AgInSbTe laser heat-mode resist, an environmental friendly and homogeneous electrochemical strategy has been explored for high throughput lithography of high-resolution diffractive optical elements.

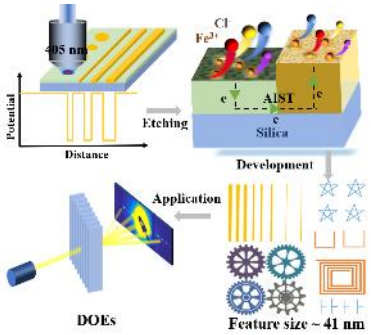

Highlights:

- An environmental friendly electrochemical strategy performed on AgInSbTe laser heat-mode resist for high-resolution and arbitrary pattern lithography
- The minimum feature sizes of lithography structure can reach to 41nm.
- Electrochemical development mechanism by the oxidization of Fe^{3+} with the assisted pitting activation of Cl^- was systematically studied.
- ~~Optical diffraction devices~~ Diffractive optical elements such as an X-ray grating were fabricated using the AIST-LHR, and showed good uniformity and diffraction properties.